

Synchrotron-based X-ray Fluorescence Ghost Imaging

MATHIEU MANNI^{1,2}, ADI BEN-YEHUDA², YISHAY KLEIN², BRATISLAV LUKIC¹, ANDREW KINGSTON³,
ALEXANDER RACK¹, SHARON SHWARTZ^{2,*}, AND NICOLA VIGANO^{1,4,**}

¹ESRF — The European Synchrotron, Grenoble, 38043, France

²Physics Department and Institute of Nanotechnology and Advanced Materials, Bar Ilan University, Ramat Gan, 52900, Israel

³Department of Materials Physics, Research School of Physics, The Australian National University, Canberra, ACT 2601, Australia

⁴IRIG-MEM, CEA, Université Grenoble Alpes, Grenoble, 38000, France

* Co-corresponding author: sharon.shwartz@biu.ac.il

** Co-corresponding author: nicola.vigano@cea.fr

Compiled August 21, 2023

X-ray Fluorescence Ghost Imaging (XRF-GI) was recently demonstrated for x-ray lab sources. It has the potential to reduce acquisition time and deposited dose by choosing their trade-off with spatial resolution, while alleviating the focusing constraints of the probing beam. Here, we demonstrate the realization of synchrotron-based XRF-GI: We present both an adapted experimental setup and its corresponding required computational technique to process the data. This extends the above-mentioned potential advantages of GI to synchrotron XRF imaging. In addition, it enables new strategies to improve resilience against drifts at all scales, and the study of previously inaccessible samples, such as liquids. © 2023 Optica Publishing Group

<http://dx.doi.org/10.1364/ao.XX.XXXXXX>

A. Introduction

X-ray fluorescence (XRF) is used in a wide variety of experimental techniques, including two-dimensional and three-dimensional chemical mapping spanning a large range of scales. It is used for sample characterization in a multitude of application areas, including material science [1], chemistry [2], and cultural heritage [3]. The chemical sensitivity of XRF is achieved through the excitation of core electrons: When the excited atoms return to lower excitation states, they emit secondary photons with characteristic energies, that uniquely depend on the atomic number. Energy-resolving detectors (routinely used in x-ray measurements), can discriminate these photons with sufficient energy resolution, to identify the element from which they originated. XRF imaging is usually achieved by scanning the samples with a focused beam (pencil beam, PB), and by collecting the emitted XRF signal (spectrum) with single-pixel energy-resolving detectors. The collected XRF spectra are then processed, to fit the measured local chemical composition [4].

PB acquisitions require raster-scanning (sequentially) of all the points in the field of view (FoV), by transversely displacing the sample. Each exposure has an associated XRF spectrum, which corresponds to one pixel in the resulting spectral image. Syn-

chrotron radiation, compared to x-ray tube-based sources, is characterized by higher photon flux and (on long beamlines) spatial coherence. This enables reaching x-ray beam waists of tens of nm with a high photon flux [5], which, in turn, enables the study of micro- and nano-structured samples with unrivaled speeds, compared to laboratory sources. As it delivers a high radiation dose rate per unit-surface per unit-time, it can cause serious localized damage and deformation in sensitive samples. Heat can also contribute to positional drifts and uncertainties, potentially leading to image degradation.

In contrast to PB, classical Ghost Imaging (GI) acquisitions illuminate the entire FoV. Differently from other full-field techniques [6, 7], it does so with different structured beams at each exposure [8]. For x-rays, these structured beams are usually obtained by inserting non-configurable transversely-displaced structuring masks in the beam, to encode the spatial information in the acquired GI signals. In the specific case of XRF-GI, the XRF detector records the spectrum associated with each illumination pattern. The XRF energy emission lines corresponding to different chemical elements are reconstructed into spatially resolved maps, using computational imaging algorithms. GI acquires spatial information on the whole FoV at each realization. Thanks to the inherent compressibility of natural images, it is possible to acquire fewer realizations than the number of pixels in the reconstructed image, leading to reduced dose deposition, which is not possible with PB scans [9]. The sole translation of the masks in XRF-GI, compared to the translation of the samples for PB, enables the study of previously inaccessible samples like liquids, that cannot move during measurements. Moreover, by spreading the beam flux over the entire FoV (as opposed to just the focal spot in PB), XRF-GI could offer more efficient mitigation of dose effects (e.g. easier cooling) and reduce the localized radiation-induced damage. Despite having first developed XRF-GI on laboratory equipment [10], the transposition to synchrotron beamlines is highly desirable, even though it comes with its own challenges.

X-ray GI image reconstructions require the mask shape and positions, and the incident beam intensity to be known. In contrast to x-ray tubes (used in laboratory x-ray setups) that are characterized by rather stable emission fluxes over time, synchrotron sources exhibit beam intensity decay. Even in top-up

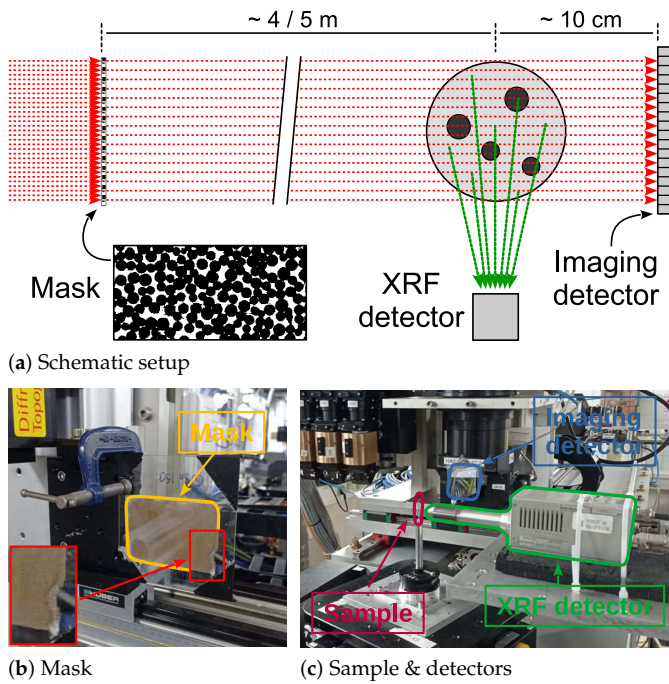


Fig. 1. (a) Schematic synchrotron XRF-GI setup; (b) CuSn mask, whose corner is shown in the inset on the bottom left; and, (c) sample, imaging detector with Si attenuation wafers, and XRF detector.

mode, flux variations of up to 10% can be observed. Beam monitors are usually placed upstream of the masks. However, the masks create unknown and variable attenuation between the diode and the sample, which renders calibration of the XRF signal difficult or impossible. The mask shapes can be known by: Measuring them before the scans or knowing their design from fabrication (Computational GI); splitting the structured beam with a beam-splitter positioned after the masks, and measuring the beam that does not impinge on the sample (Classical GI) [11–13]. On synchrotron beamlines, cameras with sub- μm or few μm pixel sizes are routinely used. With slight instability of the beam direction and sample drifts, misalignment artifacts are more likely to manifest, which negatively impacts both the above-mentioned approaches.

Here, we demonstrate a synchrotron-based XRF-GI implementation that does not require knowing or measuring the masks in advance, to split the structured beam, calibrating with high-precision the positions of the masks, nor using a beam monitor to track possible incident beam intensity variations.

B. Experimental setup

The experimental setup is presented in Fig. 1. A large structuring mask is positioned on a translation stage in the x-ray beam upstream of the sample. At each GI realization, the synchrotron x-ray beam only illuminates a portion of the mask, producing the corresponding illuminating beam shape. Different beam shapes are obtained by translating the mask transversely with respect to the incoming beam. A 2D imaging detector is positioned downstream of the sample, and an XRF single-pixel detector is positioned next to the sample, perpendicular to the incoming beam direction. We demonstrate our setup on the ID19 beamline of the ESRF — The European Synchrotron, using a $1 \times 2 \text{ mm}^2$ incident beam size. The imaging detector is a so-called Hasselblad system, with two identical lenses (100

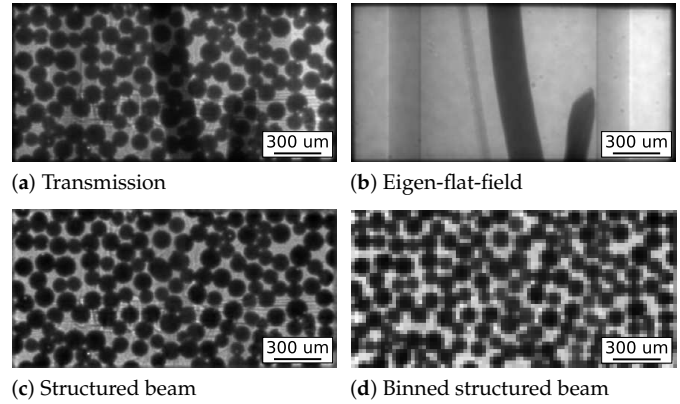


Fig. 2. (a) Transmission image of the sample with the mask; (b) eigen-flat-field computed from the stack of transmission images; (c) the extracted mask from transmission (normalized and mean-subtracted); and, (d) its 4×4 binned version. The intensity gradient in (a) and (b) is due to the fact that the sample is not correctly positioned in the center of the beam. This effect is correctly taken into account by the eigen-flat-field subtraction when retrieving (c).

mm focal length) in tandem configuration (giving $\sim \times 1$ magnification), with a $500 \mu\text{m}$ LuAG:Ce scintillator and a “Dimax pco.edge 5.5” camera. It is positioned $\sim 10 \text{ cm}$ downstream of the sample, with an effective pixel size of $6 \mu\text{m}$. A large mask, composed of a mono-layer of randomly distributed CuSn (bronze) spheres (average diameter $\sim 50 \mu\text{m}$ and maximum diameter $\sim 150 \mu\text{m}$), is positioned $\sim 4 - 5 \text{ m}$ upstream of the sample. The incoming beam energy is $\sim 26 \text{ keV}$, given by the beamline’s single-harmonic undulator (type: u13), without the use of a monochromator. The XRF detector is a “Hitachi Vortex 90EX” single-pixel detector, controlled by a “XIA FalconX” module. The sample is composed of two Cu flattened wires and one Fe $50 \mu\text{m}$ thick wire, stored in a capillary. The capillary is mostly made of plastic, with heavier trace elements.

C. Acquisition procedure

In [10], the imaging and XRF detectors acquired their respective signals separately. The sample needed to be removed from the FoV to acquire the beam structures. Thus, the same scan was performed two times, one with the sample in the FoV, using the XRF detector, and one without the sample in the FoV, using the imaging detector. This exposed one of the two measurements to positioning and flux estimation errors with respect to the other. In this new implementation, the two detectors simultaneously acquire their respective signals (for the same time duration). In other words, each XRF signal is concurrently acquired with its corresponding beam structure, in the same flux and positioning conditions, and the imaging detector records the transmitted signal through both sample and mask for each GI realization. We then separate the beam structure from the sample shape computationally, during the data processing. Both implementations require measuring the intensity distribution of the impinging beam on the mask. This is done either at the beginning or the end of the scan.

The required exposure times of the high-resolution imaging and XRF detectors are usually different: The imaging detector is exposed to the direct (intense) beam, and therefore saturates well before the required SNR is met for the XRF signal. We circumvent this by acquiring many shorter acquisitions (e.g. exposures of 0.1 s each) for each same mask position and accumu-

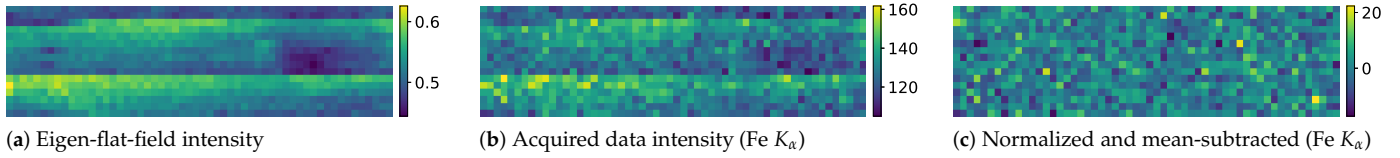


Fig. 3. (a) Integrated intensities of the eigen-flat-fields (Fig. 2b); (b) photon counts for each GI realization of the Fe K_α line; and, (c) normalized and mean-subtracted intensities for the Fe K_α line (b) by the corresponding eigen-flat-field intensities (a). Each point corresponds to one GI realization, for the 16 and 56 different positions vertically and horizontally respectively.

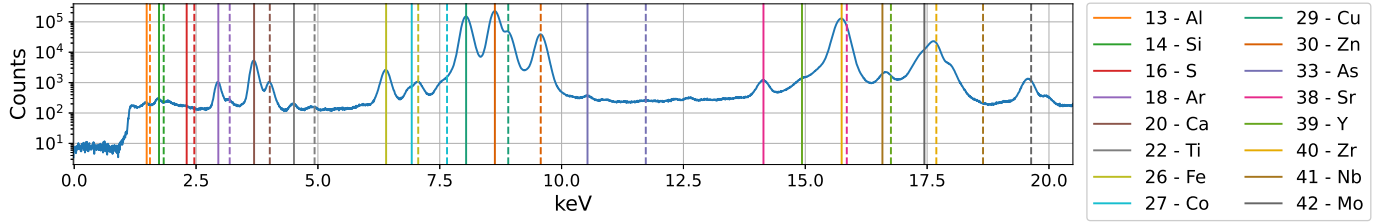


Fig. 4. XRF spectrum of the studied sample. Solid and dashed lines indicate K_α and K_β emission lines, respectively.

lating them. Here, we translated the large mask both vertically and horizontally, acquiring 16 and 56 positions respectively, at a 5 mm translation step size. This amounts to 896 total GI realizations. We exposed 32 times for each GI realization for 0.1 s, amounting to 3.2 s of cumulative realization exposure time.

D. Data processing

GI is a computational imaging technique, and it requires several computational steps to recover real-space images. Our implementation requires an additional step to decouple the structure of the incoming beam from the sample transmission, and to retrieve the normalization coefficients for the incoming beam intensity variations. In this section, we describe this additional step, which is unique to our proposed setup. We refer to Sec. C of the supp. mat. for the full GI data processing pipeline.

If we assume that the sample transmission does not change throughout the GI acquisition, it is possible to decouple the sample transmission from the beam structure through principal component analysis (PCA). Let us represent the sample transmission with the vector \underline{f} (which also includes the spatial beam intensity profile), the beam structures for each GI realization as the set of vectors $M = \{\underline{m}_j\}$, where $j \in [1, K]$ is the index of each GI realization and K is the total number of realizations, and the beam intensity for each realization with the set of coefficients $C = \{c_j\}$. For each realization, the transmission of the sample plus the structured beam is $\underline{t}_j = c_j \underline{f} \otimes \underline{m}_j$, where \otimes is the element-wise vector product. The average of all transmission images is $\frac{1}{K} \sum_j \{c_j \underline{f} \otimes \underline{m}_j\} = \underline{f} \otimes \frac{1}{K} \sum_i c_i \underline{m}_i$. The patterns in the set M are supposed to be uncorrelated with each other, and \underline{f} is the only component present in each transmission image \underline{t}_j . Thus, it is the dominant component in the PCA of the matrix $T = [\underline{t}_1, \underline{t}_2, \dots, \underline{t}_K]$. If we split the highest PCA component from the others, and reconstruct these two sets separately, we will obtain $c_j \underline{f}$ (called eigen-flat-field) from the former set, and \underline{m}_j from the latter set, for each GI realization j .

We show an example of transmission \underline{t} in Fig. 2a, the corresponding eigen-flat-field in Fig. 2b and beam structure in Fig. 2c. The intensity fluctuations c_j are computed by integrating each eigen-flat-field $c_j \underline{f}$, where $\sum_i f_i$ with $i \in [1, N]$ is the sum of all the pixels i in the image \underline{f} , and resulting in a constant multiplicative factor. The integrated intensities in Fig. 3a are in good agreement with the low-frequency trend of the corresponding Fe K_α values in Fig. 3b. We normalize the values in Fig. 3b by

the computed intensities in Fig. 3a, subtract the mean, and obtain the corrected GI realization intensities in Fig. 3c.

The GI reconstruction pixel size is determined through the auto-correlation (AC) function of the structured beams [14]. Supposing that the mask is not periodic and sampled over non-overlapping regions, the resulting structured beams are not correlated with each other. Thus, it is enough to compute the AC of each structured beam with itself. The selected GI reconstruction pixel size is the lowest half-width half-maximum (HWHM) of all the AC curves. More details can be found in the supplemental material. In the presented experiment, we found a minimum HWHM equal to 4 imaging detector pixels: Given its pixel size of 6 μm , it is equivalent to a 24 μm GI pixel size. Therefore, we binned the mask images 4×4 , as shown in Fig. 2d.

The GI reconstruction is performed with the Primal-Dual Hybrid Gradient (PDHG) algorithm, and using the l_1 -norm minimization of the isotropic Total Variation (TV) of the image [15]. The weight of the TV term is selected through cross-validation [9]. The data processing code can be found at [16].

E. Results

The XRF spectrum of the analyzed sample is shown in Fig. 4. The Fe and Cu peaks from the wires are clearly visible. The C K_α line of the plastic capillary is below the detection limit of the XRF detector, but lines of other elements can be seen, e.g. Zn. In Fig. 5, we find the GI reconstructions of the Fe, Cu, and Zn XRF signals in the FoV (Fig. 5b, Fig. 5c, and Fig. 5d respectively). In Fig. 5a, we present a color-coded composite image of the Fe, Cu, and Zn XRF signals (Red, Green, and Blue respectively), with super-imposed edges from Fig. 2b. This figure shows that the elemental images are in good agreement with the corresponding expected objects in the transmission image: The spatial distribution of the elements is correctly recovered (aside from artifacts). The two main types of artifacts are: (a) trace signals from other channels; and (b) self-attenuation. Point (a) means that the signal for one XRF line can have long tails in its energy dispersion function, and its signal can be mistakenly associated with other XRF lines. As a result, reconstructions show faint features from other elements. For instance, the Fe reconstruction (Fig. 5b) shows traces of the capillary on the leftmost part of the FoV. Point (b) means that the sample attenuates some of the XRF photons that it emits. As a result, regions of the sample further away from the detector have a much lower sig-

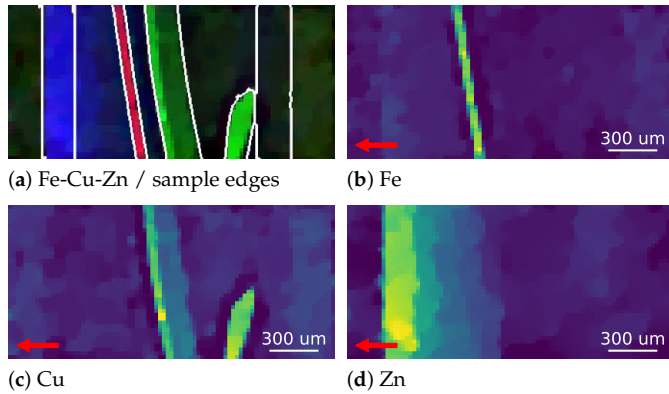


Fig. 5. (a) Composite image of Fe, Cu, Zn (Red, Green, and Blue respectively), and super-imposed edges of the transmission image in Fig. 2b; and the qualitative elemental reconstructions of: (b) Fe; (c) Cu; and, (d) Zn. The images are affected by self-attenuation of the XRF photons. The XRF detector position is indicated with a red arrow.

nal than regions of the sample closer to the XRF detector. This effect is clearly visible in both the Cu and Zn reconstructions (Fig. 5c, and Fig. 5d). More specifically, the biggest Cu wire is reconstructed with a higher signal on its left side, and only the leftmost part of the capillary is reconstructed. The XRF detector is in fact positioned on the left side of the images, as seen by the transmission detector (indicated with a red arrow in Figs. 5b to 5d). This type of artifact is common to all XRF methods. The reconstructed images are approximately $1 \times 2 \text{ mm}^2$ in size, which corresponds to 42×87 pixels (for $24 \mu\text{m}$ pixel size). The acquisition consisted of 16×56 GI realizations, which represent $\sim 24.52\%$ of the reconstructed pixels.

F. Impact & Outlook

This proof-of-concept experiment overcomes important limitations associated with a synchrotron-based GI implementation. It demonstrates XRF-GI on a synchrotron beamline, that is not otherwise suited for XRF imaging. This paves the way to enabling GI advantages (e.g. reduced dose) to synchrotron-based applications. It also enables the study of samples that could not be imaged with a PB approach, because of radiation damage or the inability to move them. This includes samples that would be perturbed by the back-and-forth translation of PB acquisitions (e.g. liquids), or with heavy sample environments that could not be displaced with enough precision or speed.

In addition, the proposed XRF-GI implementation is robust against mask positioning errors or drifts, because the structure of the beam is acquired in line with the sample (without beam splitting), and simultaneously with the XRF signal. This is not the case in other GI acquisition setups. Thus, it implies a simplified setup, with fewer sources of noise or misalignment, compared to beam-splitter-based setups or computational GI approaches. Compared to PB scanning, our XRF-GI implementation is also robust against image distortions arising from drifts during an entire acquisition. The sample is visible behind the mask at each realization, thus its position can be tracked and corrected. This could have its biggest impact at the nano-scale, where tracking drifts and positioning errors is of vital importance.

Enabling synchrotron-based XRF-GI has a direct impact on every technique that leverages the XRF signal. As an example, XAS (x-ray absorption spectroscopy) often uses XRF as a high-

quality proxy for the absorption signal. With XRF-GI, we enable obtaining spatial information from XAS measurements, without radically changing a beamline layout with respect to beam shaping and sample positioning. XAS measurements with PB scanning would experience dramatically increased acquisition time. An XRF-GI-based implementation would instead enable probing of large regions of the sample at once, with much fewer realizations (i.e. scanning points) than the number of pixels (by leveraging compressive sensing [9]). This would unlock routinely obtaining spatially resolved XAS maps within the time bounds imposed by beamtime allocation. Its applications span from the study of microscopic inclusion in macroscopic naturally occurring samples, to the observation of localized charge transfer phenomena in batteries.

In its current implementation, our technique requires that both the object and the mask are transparent enough to be both visible on the imaging detector, at the same time. This limitation can be relaxed, by scanning the mask beforehand. Even when some regions of the sample were to fully attenuate the transmitted beam, the transmission of one region of the mask in each GI realization would be enough to retrieve the correct position of the mask. This would also relax the dependency on the eigenflat-field extraction step (i.e. using PCA), especially in the presence of sample drifts during the scan.

Funding. PAZY Foundation; Australian Research Council (Discovery project, DP210101312).

Acknowledgments. AK acknowledges support from the Australian Research Council through funding of the Discovery Project DP210101312. This research was supported by the Pazy Foundation. NV acknowledges Emmanuel Brun for lending the masks, and K. Joost Batenburg, Giovanni O. Lepore, and Daniele Pelliccia for the fruitful discussion.

Disclosures. The authors declare no conflicts of interest.

Data availability. Data underlying the results are available at [17].

Supplemental document. See Supplement 1 for supporting content.

REFERENCES

1. J. A. van Bokhoven, T.-L. Lee, M. Drakopoulos, C. Lamberti, S. Thieß, and J. Zegenhagen, *Nat. Mater.* **7**, 551 (2008).
2. F. T. Haase, A. Bergmann, T. E. Jones, J. Timoshenko, A. Herzog, H. S. Jeon, C. Rettenmaier, and B. R. Cuenya, *Nat. Energy* **7**, 765 (2022).
3. R. Ploeger and A. Shugar, *Science* **354**, 826 (2016).
4. V. Solé, E. Papillon, M. Cotte, P. Walter, and J. Susini, *Spectrochimica Acta Part B: At. Spectrosc.* **62**, 63 (2007).
5. J. Cesar da Silva, A. Pacureanu, Y. Yang, S. Bohic, C. Morawe, R. Barrett, and P. Cloetens, *Optica* **4**, 492 (2017).
6. M. Vasin, Y. Ignatiev, A. Lakhtikov, A. Morovov, and V. Nazarov, *Spectrochimica Acta Part B: At. Spectrosc.* **62**, 648 (2007).
7. J. Soltau, P. Meyer, R. Hartmann, L. Strüder, H. Soltau, and T. Salditt, *Optica* **10**, 127 (2023).
8. P.-A. Moreau, E. Toninelli, T. Gregory, and M. J. Padgett, *Laser & Photonics Rev.* **12**, 1700143 (2018).
9. T. J. Lane and D. Ratner, *Opt. Express* **28**, 5898 (2020).
10. Y. Klein, O. Sefi, H. Schwartz, and S. Schwartz, *Optica* **9**, 63 (2022).
11. R. S. Bennink, S. J. Bentley, and R. W. Boyd, *Phys. Rev. Lett.* **89**, 113601 (2002).
12. D. Pelliccia, A. Rack, M. Scheel, V. Cantelli, and D. M. Paganin, *Phys. Rev. Lett.* **117**, 113902 (2016).
13. A. Gatti, E. Brambilla, M. Bache, and L. A. Lugiato, *Phys. Rev. Lett.* **93**, 093602 (2004).

14. A. M. Kingston, G. R. Myers, D. Pelliccia, F. Salvemini, J. J. Bevitt, U. Garbe, and D. M. Paganin, *Phys. Rev. A* **101**, 053844 (2020).
15. E. Y. Sidky, J. H. Jørgensen, and X. Pan, *Phys. Med. Biol.* **57**, 3065 (2012).
16. <https://github.com/cicwi/PyCorrectedEmissionCT>.
17. <https://doi.org/10.5281/zenodo.7828494>.

FULL REFERENCES

1. J. A. van Bokhoven, T.-L. Lee, M. Drakopoulos, C. Lamberti, S. Thieß, and J. Zegenhagen, "Determining the aluminium occupancy on the active T-sites in zeolites using X-ray standing waves," *Nat. Mater.* **7**, 551–555 (2008).
2. F. T. Haase, A. Bergmann, T. E. Jones, J. Timoshenko, A. Herzog, H. S. Jeon, C. Rettenmaier, and B. R. Cuenya, "Size effects and active state formation of cobalt oxide nanoparticles during the oxygen evolution reaction," *Nat. Energy* **7**, 765–773 (2022).
3. R. Ploeger and A. Shugar, "Where science meets art," *Science* **354**, 826–828 (2016).
4. V. Solé, E. Papillon, M. Cotte, P. Walter, and J. Susini, "A multiplatform code for the analysis of energy-dispersive X-ray fluorescence spectra," *Spectrochimica Acta Part B: At. Spectrosc.* **62**, 63–68 (2007).
5. J. Cesar da Silva, A. Pacureanu, Y. Yang, S. Bohic, C. Morawe, R. Barrett, and P. Cloetens, "Efficient concentration of high-energy x-rays for diffraction-limited imaging resolution," *Optica* **4**, 492 (2017).
6. M. Vasin, Y. Ignatiev, A. Lakhtikov, A. Morovov, and V. Nazarov, "Energy-resolved X-ray imaging," *Spectrochimica Acta Part B: At. Spectrosc.* **62**, 648–653 (2007).
7. J. Soltau, P. Meyer, R. Hartmann, L. Strüder, H. Soltau, and T. Salditt, "Full-field x-ray fluorescence imaging using a Fresnel zone plate coded aperture," *Optica* **10**, 127 (2023).
8. P.-A. Moreau, E. Toninelli, T. Gregory, and M. J. Padgett, "Ghost imaging using optical correlations," *Laser & Photonics Rev.* **12**, 1700143 (2018).
9. T. J. Lane and D. Ratner, "What are the advantages of ghost imaging? Multiplexing for x-ray and electron imaging," *Opt. Express* **28**, 5898 (2020).
10. Y. Klein, O. Sefi, H. Schwartz, and S. Shwartz, "Chemical element mapping by x-ray computational ghost fluorescence," *Optica* **9**, 63 (2022).
11. R. S. Bennink, S. J. Bentley, and R. W. Boyd, "'two-photon' coincidence imaging with a classical source," *Phys. Rev. Lett.* **89**, 113601 (2002).
12. D. Pelliccia, A. Rack, M. Scheel, V. Cantelli, and D. M. Paganin, "Experimental X-Ray Ghost Imaging," *Phys. Rev. Lett.* **117**, 113902 (2016).
13. A. Gatti, E. Brambilla, M. Bache, and L. A. Lugiato, "Ghost imaging with thermal light: Comparing entanglement and classical correlation," *Phys. Rev. Lett.* **93**, 093602 (2004).
14. A. M. Kingston, G. R. Myers, D. Pelliccia, F. Salvemini, J. J. Bevitt, U. Garbe, and D. M. Paganin, "Neutron ghost imaging," *Phys. Rev. A* **101**, 053844 (2020).
15. E. Y. Sidky, J. H. Jørgensen, and X. Pan, "Convex optimization problem prototyping for image reconstruction in computed tomography with the Chambolle-Pock algorithm," *Phys. Med. Biol.* **57**, 3065–3091 (2012).
16. <https://github.com/cicwi/PyCorrectedEmissionCT>.
17. <https://doi.org/10.5281/zenodo.7828494>.